Fast photoacoustic imaging systems using pulsed laser diodes – a review

Paul Kumar Upputuri, and Manojit Pramanik*
School of Chemical and Biomedical Engineering, Nanyang Technological University, 62 Nanyang Drive, Singapore 637459

Abstract. Photoacoustic imaging (PAI) is a newly emerging imaging modality for preclinical and clinical applications. The conventional PAI systems use Q-switched Nd:YAG/OPO (Optical Parametric Oscillator) nanosecond lasers as excitation sources. Such lasers are expensive, bulky, and imaging speed is limited because of low pulse repetition rate. In recent years, the semiconductor laser technology has advanced to generate high-repetitions rate near-infrared pulsed lasers diodes (PLDs) which are reliable, less-expensive, hand-held, and light-weight, about 200 gm. In this article, we review the development and demonstration of PLD based PAI systems for preclinical and clinical applications reported in recent years.

Keywords: Photoacoustic tomography, Photoacoustic microscopy, Pulsed laser diode, Ultrasound system, Clinical translation, *In vivo* imaging

Address all correspondence to: Manojit Pramanik, School of Chemical and Biomedical Engineering, Nanyang Technological University, 62 Nanyang Drive, Singapore 637459; Tel: +65-6790-5835; Fax: +65-6791-1761; E-mail: manojit@ntu.edu.sg

1 Introduction

In the last couple of decades, a new biomedical imaging modality known as optoacoustic imaging (OAI) or photoacoustic imaging (PAI) is progressing from bench to bedside [1-12]. PAI provides structural, hemodynamics, functional, oxygen metabolism, gene expressions, biomarkers, molecular, etc. [12-14]. Due to these advantages, PAI modality is finding many applications in oncology, dermatology, cardiology, etc. [12, 15]. PA imaging utilizes the advantages of both ultrasound (US) and optical imaging methods. In photoacoustic imaging, laser pulse, typically a nanosecond pulse, irradiates the tissue sample. The tissue chromophores (oxyhemoglobin [HbO2], deoxyhemoglobin [Hb], water, lipids, melanin, collagen, DNA/RNA, etc.) absorb the incident light, resulting in rise of temperature locally. The temperature rise produces sound waves, known as photoacoustic waves. These PA waves

were acquired from the tissue boundary to form a cross-sectional image. PAI has several advantages compared to optical or ultrasound imaging techniques [3, 16-23]: (i) it is a multi-scale multi-contrast label-free imaging modality, (ii) it can provide longer penetration depths in soft-tissues compared to pure optical methods, (iii) speckle artifacts are not present in PA imaging, (iv) PAI systems are less expensive compared with other clinical imaging systems like X-ray imaging, magnetic resonance imaging (MRI), positron emission tomography, tec. (v) PAI can provide anatomical, functional, and molecular information, (vi) The sensitivity of PAI is 2 orders of magnitude more than that of OCT and confocal microscopy.

Broadly photoacoustic imaging systems can be classified as: (i) photoacoustic tomography (PAT) [1, 24-31], (ii) photoacoustic microscopy (PAM) [32-50], (iii) photoacoustic endoscopy (PAE) [51-54]. In PAT systems usually an expanded high energy laser short pulses irradiates the test sample and photoacoustic signals are collected outside tissue using ultrasound transducers (USTs). The collected photoacoustic signals can be used to generate a cross-sectional image the initial pressure rise (representing the absorption coefficient) within the tissue. PAT is a deep-tissue imaging modality. With the help of contrast agent an imaging depth of ~11.6 cm was achieved in biological tissues with the 1064 nm laser power of 56 mJ/cm^2 [55, 56]. In photoacoustic microscopy, both the light beam and acoustic detection are focused in confocal geometry. PAM is classified into AR-PAM (AR stands for acoustic resolution) [57-60] or OR-PAM (OR stands for optical resolution) [61-68]. In acoustic resolution PA microscope acoustic focus is finer whereas in optical resolution PA microscope optical focus is finer. PAM can provide better imaging depth (~1 cm) compared to optical microscopy [69]. PAE can provide deeper imaging than optical endoscope. It can be used to image esophagus, colon etc. An imaging depth of 7 mm was achieved *ex vivo* in the rat colon

using PAE [70]. Photoacoustic microscopy and endoscopy are limited to surficial imaging applications.

The photoacoustic excitation pulse duration needs to be less than the thermal and stress confinement times. So typically near-infrared (NIR)/visible (VIS) laser pulses with duration nanosecond were used to excite tissue samples. Traditional high energy excitation lasers used for PAT are expensive, non-portable, and have low-repetition rate (~10-100 Hz). The limited pulse repetition rate is an issue for dynamic imaging of tissues such as beating heart. Such lasers prevent the PAI technique from being widely introduced into clinics. 1064 nm or 532 nm Nd:YAG lasers provide economical option, but their fixed wavelength strongly limits their application to anatomical imaging. Moreover, near infrared (NIR) window providing deeper light penetration in tissue made 650-900 nm wavelength window a commonly used one in PAT for deep tissue imaging [3, 71]. In recent years, pulsed laser diode (PLD) [24, 29, 72-75] or light emitting diode (LED) [76-78] were used as a substitute to conventional Nd:YAG/OPO laser due to the fact that they are less expensive, reliable, ultra-compact, and can provide thousands of pulses in a second for real-time imaging. Demonstration of PLD based PAI systems in various applications, such as, brain imaging [24, 79], rheumatology [80], high-frame rate imaging [81], and the diagnosis of cardiovascular disease [82] has already been successfully performed.

In this review, we discuss the current status and progress in photoacoustic imaging systems with the PLD excitation and its applications in clinical practices. This review article is structured in this manner: Sec-2 presents main components of PAI systems; In Sec-3 we

discuss about conventional photoacoustic tomography systems; Sec-4 is dedicated to PLD-PAT systems; Sec-5 is dedicated to PLD based PAM systems; In Sec-6, we will discuss the PLD based clinical ultrasound systems and its applications; and in Sec-7, we will conclude the review, and discuss about the future directions for the advancement of PAI system technology.

2. Main components of PAI systems

The main components of photoacoustic imaging systems are described in Fig. 1. They are excitation sources, light delivery systems, ultrasound transducers, and image formation. Technological advancement of all these components will make the PAI system an ideal tool for preclinical and clinical studies. The excitation laser for PAI is usually a nanosecond visible/near-infrared laser source. The pulsed diode laser and light emitting diode technologies have advanced to produce nanosecond pulses in near-infrared wavelength range. PLD and LED lasers were successfully demonstrated for both clinical and preclinical PA imaging. However, the PLD and LED technology yet to be developed to generate high energy and tunable output for deep-tissue and spectroscopic imaging applications.

Light delivery system can be defined as system for controlling the light transportation from an excitation light source to a target/tissue. In PAI imaging systems, light delivery was achieved by free-space optics (reflecting surfaces, such as, mirrors or prisms, etc.), fiber based optics (single/multi-mode fiber, fiber bundle, etc.), focusing optics (short focal length converging lenses or microscopic objectives, etc.), and light scanning devices (Galvo mirrors [83] or MEMS mirrors [84-87]).

Various devices have been developed for detecting the PA signals. A Fabry-Perot polymer film etalon was used to detect PA signal from DC to several tens of MHz [88, 89]. The PZT (Lead Zirconate Titanate) based transducers have been widely used in PAI systems because they are cheaper and readily available in the market (most commercial ultrasound transducers used in clinical ultrasound system uses PZT transducers). Single-element USTs with central frequency (fc) 1 MHz to ~1.2 GHz [90, 91], 45 MHz 1-D array USTs, and 70 MHz 2-D array USTs have been used in PAT or PAM systems [91]. PZT based USTs can provide high sensitivity, 70-80% bandwidth, low-cost, and best for dual modal PA/US imaging. New US detection technologies based on PVDF (plyvinylidene diflouride), and CMUT (Capacitive-micromachined ultrasound tansdcer) have been explored for PA imaging. PVDF based one is high sensitive than PZT, shape flexible, and not usable as US emitter. CMUT based transduceres have highest band width, senitivity same as PZT, but cross talk between the arrays and dieleltric charging are challenging issues [92-94].

Several reconstruction algorithms have been development in parallel for PA image formation and display: (a) a model-based reconstruction [95-98], (b) filtered-back-projection algorithm [99], (c) single-stage algorithm [100], (e) pulse decomposition algorithm [101], (e) focal-line-based 3-D image reconstruction algorithm [102], (e) a multi-view Hilbert transformation [103], (f) algorithm based on compressed sensing [104], and (g) simple delay-and-sum algorithm [105, 106]. Some of these reconstruction algorithms are computationally expensive and slow, therefore, efforts are ongoing for developing fast, efficient, real-time reconstruction methods.

3. Conventional photoacoustic tomography (PAT) system

In conventional PAT systems, high-energy laser beam from Nd:YAG/OPO laser is expanded to irradiate the test sample homogeneously, and PA signals emitted by the sample are collected by circularly rotating the single element UST in a stop-and-go manner. The diagram of a conventional PAT system is shown in Fig. 2 [29]. The excitation laser used in this system was an optical parametric oscillator (Surelite OPO) from Continuum, and a 1064 nm/532 nm Nd:YAG pump laser (Surelite Ex) from Continuum. The excitation source delivers 10 pulsed in one second with each having pulse duration 5 ns. The signal wavelength of OPO can be changed from 670 nm to 970 nm. The output of OPO was associated with the residual 532 nm beam, to eliminate that a 590 nm long pass filter from Thorlabs (LGL590) was used in the OPO beam path. Then the OPO NIR output beam was guided by the P1, P2 right angle prisms and L1, L2 long focal length focusing lenses to the circular UST scanner. Another focusing lens L3 was used to expand the narrow beam to illuminate the region of interest. A ground glass (GG) was used to achieve homogeneous illumination on the tissue surface. The system could provide laser fluence on tissue surface up to ~18 mJ/cm^2 which is within the ANSI maximum permissible exposer (MPE) [107]. UST with central frequency 2.25 MHz was incorporated in the system to collect signals. PA signals thus detected by the UST were amplified, and filtered (1-10 MHz band pass) by the pulser/receiver unit (R/A/F) from Olympus-NDT (5072PR). Finally, the digitized signals were saved by the computer. The compute is equipped with a 25 Ms/s DAQ (data acquisition) card from GaGe (compuscope 4227).

In conventional PAT systems, data acquisition was achieved in 2 different approaches. One is stop-and-go scanning [108], and another is continuous scanning [109]. In stop-and-go approach the motor rotates the detector through an angle, acquires several PA signals,

averages the signals for better signal-to-noise ratio, saves the averaged PA signals, and moves the detector further to some new position. In continuous scanning approach, the motor rotates the detector continuously at constant speed, while the detector is moving signals are collected, and finally when the rotation is completed the signals are saved. If required, PA signals can be averaged after data acquisition. Compared to the stop-and-go method continuous scanning method can acquire data faster. But, before scanning one should consciously select the scanning time (it is the total acquisition time within which all the A-lines were acquired to generate a cross-sectional image) when system is operating in continuous scanning mode which otherwise results in image blur. This blur could be due to detector motion or due to averaging. For good quality imaging, the magnitude of blur should not be greater than the lateral resolution or test sample size.

Although, the traditional lasers can provide high energy pulses for better penetration depths in photoacoustic imaging, these lasers are costly, large in size (active vibration isolation optical table), cannot be used for high-speed or real-time imaging with single detector scanning. If such lasers are used, typically, it takes few minutes to generate one good quality *in vivo* image. On the other hand, portable optical parametric oscillator based lasers are even more expensive than non-portable OPO lasers [110, 111]. In recent years, pulsed laser diode (PLD) was widely used as an excitation source in PAT as well as PAM systems. PLD could make PAI a simple, affordable and yet efficient tool for both small animal imaging and clinical applications. Below sections we will discuss the recent advances in PLD based PAI systems and their applications.

4. PLD based PAT systems

4.1 Fiber-coupled PLD as an excitation source

A circular scanning-based PAT system using fiber-coupled PLD as an excitation source was reported and shown in Fig. 3(a) [74]. The excitation source consists of four PLDs. The specifications of this PLD are wavelength (λ) ~905 nm, pulse repetition rate (RR) ~2 kHz, pulse width (PW) ~500 ns. It can also provide 65 ns pulses at high repetition rate 20 kHz. The output of each PLD was coupled to an optical fiber with core diameter 1.5 mm to deliver the light from PLD to the sample to be imaged. A phantom shown in Fig. 3(b) was imaged to prove that the system could be used for 2D imaging. The phantom has 3 absorbers (diameter ~2.7 mm, thickness ~1 mm, absorption coefficient μ_a = 1 mm^{-1}, which is similar to blood). The phantom was illuminated by the PLD output from fiber bundle. A 3.5 MHz focused UST was scanned around the phantom with a scanning radius 25 mm. The UST was rotated in 306° with each step 3.6°. The PLD-PAT images of the phantom with 500 ns and 65 ns pulses are shown in Figs. 3(c) and 3(d), respectively. These images were compared with the image [Fig. 3(e)] obtained with 7 ns Nd:YAG/OPO laser. In this work, the authors concluded that the fiber-coupled PLD-PAT system can provide 2D images and it can be used for surface or subsurface imaging applications such as visualizing superficial vascular anatomy. In this work, UST was not scanned in full circle. The stop-and-go approach (discussed in section-3) which is time-consuming was used to acquire PA signals. The PLD output is highly diverging, using fiber will make it easy to deliver light form source to the sample, but the PLD pulse energy will be significantly reduced due to fiber.

4.2 Free-space pulsed laser diode as an excitation source

A PAT system using free-space PLD was reported in different design [29, 79]. In this work, the PLD was integrated inside the scanner so that no additional optics is required and hence

no loss of energy. Continuous scanning was used to make data acquisition faster. Along with imaging resolution, high-speed, deep-tissue, *in vivo* imaging capabilities of PLD-PAT were reported in this work. The schematic of the PAT system based on free-space PLD is shown in Fig. 4(a). The photograph of the set-up is presented in Fig. 4(b). The laser diode is from Quantel, France. It is capable of providing ~136 ns pulses at wavelength of ~803 nm. The maximum pulse energy available at laser window 1.42 mJ at 7000 Hz pulse rate. To make the PLD output beam uniform, a ground glass (GG) was used in front of PLD window. The driving unit (LDU) controls the PLD output power and repetition rate. The LDU consisted of a device (MTTC1410) to control temperature from LaridTech, a power supply unit (12V, PPS-11810) from Voltcraft, another tunable power supply (BT-153) from BASETech, and a simple function generator (FG250D) from Funktionsgenerator. This generator can provide a TTL signal to sync DAQ card with PLD pulsing. A cylindrically focused transducer from Olympus NDT (V306-SU-NK-CF1.9IN) with central frequency 2.25 MHz, focal length of ~4.83 cm, and 13 mm active area was used in the system to acquire A-lines. A motor (SM) from Lin Engineering (Silverpak 23C) was used to rotate the detector in a circular motion around the test target. The acquired A-lines were amplified, and filtered with 1- 10 MHz band filter by US pulser/receiver unit (R/F/A). The digitized signals were saved by the computer with 25 Ms/s data acquisition card from GaGe (compuscope 4227). Table-1 compares the performance of pulsed laser diode based PAT system against conventional Nd:YAG/OPO-PAT system [29, 112]. The system could provide better quality images in just 3 sec and ~2 cm imaging depth in chicken breast tissue. Later *in vivo* small animal imaging was demonstrated using the PLD based PAT system [79].

For *in vivo* animal experiments, female rats having body weight 95±3 gm were used. Before placing the animal in the scanner, the hair on the scalp are was removed [79]. The rat brain area to be imaged was adjusted so that it is at the center of both the scanner and laser beam. The continuous scanning approach (discussed in section-3) which can make data acquisition faster was used to collect photoacoustic signals from the rat brain. The PA signal from brain vasculature was pre-amplified with 50 dB gain, thus multiple signals were acquired around the brain area. To compare the effect of scan speed on the quality of image, A-lines at different scan times were acquired. The picture of the cortex with scalp and without scalp are shown in Figs. 4(c) and 4(d), respectively. All images were acquired non-invasively with skin and skull intact. The high-speed images of the cortical vasculature of the brain in scan times 5 sec, and 30 sec are shown in Figs. 4(e), and 4(f), respectively. Even at such high speed imaging, all the frames show superior sagittal sinus (SS), transverse sinuses (TS) clearly, and fine cerebral veins (CV) on the cortex are also visible. For images acquired at different scan speeds, the signal-to-noise ratio (SNR) was calculated and plotted against scan time as shown in Fig. 4(g). The SNR of the brain image was calculated with the well-known relation, $SNR=V_{pp}/SD_n$, where V_{pp} is the peak-to-peak photoacoustic signal amplitude, and SD_n is the standard deviation of the background noise. The outcome of this experiment proved that 5 sec scan-time was enough to obtain good quality in vivo brain images with PLD-PAT system.

PAT system has been widely used for the characterization of pharmacokinetics and, distribution of biomaterials in the making process of contrast agents or drugs in small animal studies [55, 113-117]. The pharmacokinetics of ICG (Indocyanine green) was studied in the cortex of rat brain using the PLD-PAT system [79]. The rat cortex was imaged in 5 sec scan time. Indocyanine green from Sigma-Aldrich (12633-25 mg) was injected through the tail

vein. After injecting the ICG in to the blood stream, the uptake as well as the clearance process of ICG was visualized by the PLD-PAT system in the vasculature of the brain. Figure 4(h) shows the brain vasculature with poor contrast before the administration of ICG. ICG (0.3 ml) with 323 µM concentration which can absorb PLD laser wavelength was administered through tail vein [29]. Figure 4(i) shows the brain vasculature 2 min after the administration of ICG. Figure 4(j) shows the pharmacokinetics of ICG in the superior sagittal sinus of rat brain. It is similar to the trend reported in Ref [118]. The PA signal was maximized around ~2 min post-injection time and ICG was cleared from the rat body in about 15 min after injection. For this study, one brain image was acquired in every ~30 sec. In this 30 sec, PLD was ON for 5 sec for imaging and PLD was OFF for the rest 25 sec. The temporal resolution of the system can be enhanced by using multiple transducers. If 'N' number of USTs are used, one can rotate just 360/N degrees instead of 360 deg. For example, if N=8, then the frame rate of imaging system would be 1 frame per ~0.5 sec.

5. PLD based PAM systems

Photograph of OR-PAM system with a near-infrared (NIR) PLD is shown in Fig. 5(a) [119]. The PLD (905D4S16C, Laser Components, Montreal, Canada) with specifications λ ~905 nm, PW ~100 ns, RR = 0.8 kHz, PE ~4.9 µJ was the excitation source. A compound lens with numerical aperture (NA) 0.62 and focus length 15 cm was used to focus the PLD beam on to the sample. The individual components of the NIR PLD based OR-PAM system are shown in Fig. 5(b). A dead ant with a length of ~3.5 mm and diameter of ~0.7 mm was selected as the sample. The schematic of the ant is shown in Fig. 5(c). Figures 5(d) and 5(e) show the two-dimensional PAM images of dead ant acquired using 4.53 MHz UST. The images displayed characteristics of spatial shape and size of the ant. Later, visible (VIS) PLD was demonstrated

as an excitation source for OR-PAM [120]. The PLD (SLD3237VFR, Sony, Japan) with specifications λ ~405 nm, PW ~174 ns, RR = 1 kHz, PE ~52 nJ was the excitation source. OR-PAM images of carbon fibers acquired using 3.6 MHz UST are shown in Figs. 5(f) and 5(g). The surface flaws of fiber are clearly visible in the images.

Very recently another PLD based OR-PAM system in both transmission mode and reflection mode was reported [121]. Schematic of the reflection mode PLD-PAM system is shown in Fig. 6(a). OR-PAM images of black tape phantom are shown in Figs. 6(b-d). The samples were scanned by a motorized X-Y scanner with 100 pixels X 100 pixels and a step size of 100 μm. This system could provide PA signal from black tape with signal-to-noise ratio (SNR) ~6.5 dB. To generate meaningful PA image, 500 times averaging of the PA signals was performed. *Ex vivo* OR-PAM image of mouse ear acquired in about 12 min is shown in Figs. 6(e-f). After averaging 5000 times, the SNR of the PA signal was 2 dB. The number of scanning points used were 50 pixels X 50 pixels with a step size of 100 μm. Thus, the pulsed NIR or VIS PLDs can serve a low-cost compact excitation source for PAM systems and can be employed for biological tissue imaging and may represent a potential development direction for superficial biomedical applications.

6. PLD based PA/US systems and their applications

Ultrasound imaging systems used in clinics are FDA approved devices. These systems are routinely used by the doctors and technologists in the clinics. Photoacoustic imaging is different from ultrasound imaging, but both share the same ultrasound receiving mechanism. Therefore the photoacoustic imaging capabilities can be easily incorporated in to the clinical

US system which will provide dual modal imaging. In the sections below we will discuss the PLD based clinical US systems and their applications. Demonstration of such systems in various applications, such as high-frame rate imaging [81], rheumatology [80], and the diagnosis of cardiovascular disease [82] have already been successfully performed .

6.1 High-frame rate photoacoustic imaging

Recently, by combing 7000 Hz PLD source with ultrasound system from Alpinion, South Korea (ECUBE 12R), a frame rate of 7000 Hz was demonstrated on phantoms [81]. The picture of the PLD integrated US system is presented in Fig. 7(a). This PLD source is same as the one mentioned in Section-4.2. The wide laser diode beam was focused using a cylindrically focusing lens to irradiate 150 mm X 5 mm area. The energy density in this area was maintained at 1.87 mJ/cm^2. A L3-12 linear array transducer from Alpinion (fc = 8.5 MHz, 95% BW) was used in the system. It has 128 array elements to acquire PA/ultrasound signals generated from the sample. The array element pitch is 300 μm and elevation height is 4500 μm. The sampling frequency of Ecube system is 40 MHz, it has 12 bit ADC, and it can transfer data at a speed of 6 Gb/s. This system can provide raw PA data for PA image processing and analysis. It can display the ultrasound/PA images in real-time.

The L3-12 transducer can work in two modes, Mode-1 and Mode-2. In Mode-1, all the 128 arrays elements are used whereas in Mode-2 only 64 (1-64 or 65-128) channels elements are used. To demonstrate high-frame rate photoacoustic imaging, experiments on imaging liquids at different flowrates was carried out. The system could record 3500 fps when operated in Mode-1, and 7000 fps when operated in Mode-2. The PA images of ink flowing inside a

LDPE are shown in Figs. 7(b-i). The transducer was operating in Mode-2. The inner diameter of the tube was 1.15 mm. When operated at 7000 fps, 350 frames were recorded in 0.05 s. Images in Figs. 7(b-e) correspond to 3 cm/s flow rate, whereas images in Figs. 7(f-i) correspond to 14 cm/s flow rate. These results prove that it is possible to achieve high frame rate PA B-scan imaging with the Ecube US system integrated with high-repetition rate PLD. Similar experiments were performed with the Q-switched Nd:YAG/OPO laser having repetition rate 10 Hz, and it was demonstrated that only 10 fps PA imaging was possible due to low pulsing rate of the laser. Theoretically, the flow rate that can be measured using 7000 fps frame rate is up to 134.4 m/s. Further investigations are required to find out the possible *in vivo* applications of high frame rate photoacoustic imaging, like imaging CTCs (circulating tumor cells), blood vessel, heart valves, etc.

6.2 Rheumatology

A near-infrared PLD was smartly integrated inside an ultrasound probe for PA/US imaging of human finger joints. The picture of the system is presented in Fig. 8(a) [80, 122]. The system used an ultrasound probe (Esaote SL3323) having 128 elements, each with 0.245 mm pitch and 5 mm length. The transducer array has 7.5 MHz central frequency, and 100% bandwidth at −6 dB. An acoustic lens is used in the transducer array to focus the ultrasound in the elevation plane at a distance of 20 mm. The PLD source used is from Quantel (Paris, France) and its specifications are λ ~805 nm, PW ~130 ns, RR = 10 kHz, PE = 0.56 mJ/pulse at laser window. The output of the PLD was not homogenous and has large divergence angle. To make the beam homogenous a fused silica diffuser with optical efficiency 80% was used. The system can provide energy density ~1.3 mJ/cm^2 in 18.2 × 2.3 mm^2 skin area. When operated in dual (PA/US) mode, the system could provide photoacoustic imaging at a frame rate of 10 fps (each frame is an average of 20 images) and US imaging at a frame rate of 80 fps

(without averaging), respectively. The sagittal [Fig. 8(b)] and transverse plane [Fig. 8(c)] of a human proximal interphalangeal (PIP) joint images contain both ultrasound (gray) and photoacoustic (yellowish red) contrast. Ultrasound could show skin on the human finger, bone, and joint gap, whereas the skin and blood vessels are seen in photoacoustic images. The deeper PA signals are due to the reflection of skin photoacoustic signal on bone. The outcome of the study promises that this bedside device has a potential to visualize rheumatoid arthritis in human finger joints.

6.3 Cardiovascular diseases

PAI can be used in the diagnosis of atherosclerosis by identifying whether a matured carotid plaque is potentially vulnerable to rupture. When a rupture occurs, the content of the lesion that enters the blood stream can cause a stroke. Improved diagnosis and risk assessment of plaques after their initial detection could lead to a reduction of these plaque-induced strokes. It also could avoid unnecessary surgeries for patients with a stable plaque. A demonstration of *ex vivo* imaging to identify intraplaque hemorrhages in carotid plaques using PA/US imaging system [Fig. 9(a)] was reported [82]. A handheld PA/US probe incorporated with a PLD source was used in the system. This probe has an integrated pulsed laser diode (λ ~808 nm, PW ~130 ns, PE = 1 mJ, RR = 2 kHz from Quantel, France) and a linear array ultrasound transducer (SL3323, fc = 7.5 MHz, ESAOTE Europe, Maastricht, The Netherlands). The system has 500 μm lateral resolution and 280 μm in the axial resolution. *Ex vivo* imaging to identify intraplaque hemorrhages in carotid plaques using photo-acoustics was demonstrated [82]. Their study showed a good correlation between hemorrhage locations visualized from histology sections of the plaque and the photoacoustic signal from a laser diode at 808 nm Fig. 9(b). This study is a first step to prove that PAT can also be as a tool to reduce plaque-

induced strokes. However, further investigations are needed to use this PLD-PA/US system in clinics to diagnose cardiovascular diseases.

7. Conclusions and future directions

In this review we talked about the progress in PLD based photoacoustic imaging systems and its applications from preclinical to clinical practices. Compared to Q-switch Nd:YAG lasers PLDs are low-cost, reliable, light-weight, and can generate pulses at high repetition rate. Development of PLD based PAI systems and their applications for small animal brain imaging, high frame rate imaging, Rheumatology, and diagnosis of cardiovascular diseases are discussed. Progress in PLD technology led the PAI system technology to progress from preclinical to clinical, from static to dynamic, and from expensive to affordable device. However, PLDs so far demonstrated for PA imaging still have several drawbacks: (a) Beam quality: The PLD output beam suffers from bad beam quality. Optical diffuser needs to be used to achieve homogenous illumination in PLD-PAT systems. In PLD-PAM systems, achieving fine focal spot (which effects the lateral resolution) is difficult due to poor beam quality. (b) Beam divergence: PLD output beam is highly diverging, and requires additional optics or fiber to deliver the beam to the sample. (c) Pulse energy: PLDs can deliver pulses with energy about 1 mJ at laser window, it is 100 times less than the energy of typical Nd:YAG/OPO laser pulse. Such low pulse energy seriously effects the imaging depth. (d) Single wavelength: PLDs can deliver single wavelength limiting its applications to anatomical imaging. Multiple wavelengths are required for functional imaging or spectroscopic applications. (e) PLD size: the high-power PLDs are not miniature enough to be packaged inside an ultrasound probe or an endoscope. (f) Most of the commercially available high power PLDs are not emitting visible wavelength which will limit its

applications in VIS-PAI systems. On the other hand, researchers have started using light emitting diodes (LEDs) in PAI systems [77, 78, 123-125]. The LEDs are available in visible range, and hence can be used to imaging the biology tissue which contains chromophores which can absorb visible light. However, further investigations are needed to mature PLD and LED laser technology to be used in clincial imaging systems.

8 Acknowledgement

The authors would like to acknowledge the financial support from the Singapore Ministry of Health's National Medical Research Council (NMRC/OFIRG/0005/2016: M4062012). Authors have no relevant financial interests in the manuscript and no other potential conflicts of interest to disclose.

References

[1]. Li L, Zhu L, Ma C, Lin L, Yao J, Wang L, Maslov K, Zhang R, Chen W, Shi J. Single-impulse panoramic photoacoustic computed tomography of small-animal whole-body dynamics at high spatiotemporal resolution. Nature Biomedical Engineering. 2017; 1:0071.

[2]. Deán-Ben XL, Fehm TF, Ford SJ, Gottschalk S, Razansky D. Spiral volumetric optoacoustic tomography visualizes multi-scale dynamics in mice. Light: Science & Applications. 2017; 6(4):e16247.

[3]. Upputuri PK, Pramanik M. Recent advances toward preclinical and clinical translation of photoacoustic tomography: a review. J Biomed Opt. 2017; 22(4):041006.

[4]. Manohar S, Razansky D. Photoacoustics: a historical review. Advances in Optics and Photonics. 2016; 8(4):586-617.

[5]. Wang LV, Yao J. A practical guide to photoacoustic tomography in the life sciences. Nat Methods. 2016; 13(8):627-38.

[6]. Zhou Y, Yao J, Wang LV. Tutorial on photoacoustic tomography. J Biomed Opt. 2016; 21(6):061007.

[7]. Kim J, Park S, Jung Y, Chang S, Park J, Zhang Y, Lovell JF, Kim C. Programmable Real-time Clinical Photoacoustic and Ultrasound Imaging System. Sci Rep. 2016; 6:35137.

[8]. Mathiyazhakan M, Upputuri PK, Sivasubramanian K, Dhayani A, Vemula PK, Zou P, Pu K, Yang C, Pramanik M, Xu C. In situ synthesis of gold nanostars within liposomes for controlled drug release and photoacoustic imaging. Science China Materials. 2016; 59(11):892-900.

[9]. Taruttis A, Ntziachristos V. Advances in real-time multispectral optoacoustic imaging and its applications. Nat Photonics. 2015; 9(4):219-27.

[10]. Upputuri PK, Sivasubramanian K, Mark CSK, Pramanik M. Recent developments in vascular imaging techniques in tissue engineering and regenerative medicine. BioMed Research International. 2015; 2015:9.

[11]. Wang LV, Gao L. Photoacoustic microscopy and computed tomography: from bench to bedside. Annu Rev Biomed Eng. 2014; 16:155-85.

[12]. Wang LV, Hu S. Photoacoustic Tomography: In Vivo Imaging from Organelles to Organs. Science. 2012; 335(6075):1458-62.

[13]. Zhang YM, Jeon M, Rich LJ, Hong H, Geng JM, Zhang Y, Shi SX, Barnhart TE, Alexandridis P, Huizinga JD, Seshadri M, Cai WB, Kim C, Lovell JF. Non-invasive multimodal functional imaging of the intestine with frozen micellar naphthalocyanines. Nat Nanotechnol. 2014; 9(8):631-8.

[14]. Kim C, Favazza C, Wang LV. In vivo photoacoustic tomography of chemicals: high-resolution functional and molecular optical imaging at new depths. Chem Rev. 2010; 110(5):2756-82.

[15]. Jeon M, Kim J, Kim C. Multiplane spectroscopic whole-body photoacoustic imaging of small animals in vivo. Med Biol Eng Comput. 2016; 54(2-3):283-94.

[16]. Upputuri PK, Pramanik M. Microsphere-aided optical microscopy and its applications for super-resolution imaging. Opt Commun. 2017; 404:32-41.

[17]. Lee D, Lee C, Kim S, Zhou Q, Kim J, Kim C. In Vivo Near Infrared Virtual Intraoperative Surgical Photoacoustic Optical Coherence Tomography. Sci Rep. 2016; 6:35176.

[18]. Upputuri PK, Pramanik M, Nandigana KM, Kothiyal MP. Multi-colour microscopic interferometry for optical metrology and imaging applications. Optics and Lasers in Engineering. 2016; 84:10-25.

[19]. Kim J, Lee D, Jung U, Kim C. Photoacoustic imaging platforms for multimodal imaging. Ultrasonography. 2015; 34(2):88-97.

[20]. Upputuri PK, Wu Z, Gong L, Ong CK, Wang H. Super-resolution coherent anti-Stokes Raman scattering microscopy with photonic nanojets. Opt Express. 2014; 22(11):12890-99.

[21]. Upputuri PK, Gong L, Wang H. Chirped time-resolved CARS microscopy with square-pulse excitation. Opt Express. 2014; 22(8):9611-26.

[22]. Upputuri PK, Lin J, Gong L, Liu X, Wang H, Huang Z. Circularly polarized coherent anti-Stokes Raman scattering microscopy. Opt Lett. 2013; 38(8):1262-64.

[23]. Upputuri PK, Wang H. A picosecond near-infrared laser source based on a self-seeded optical parametric generator. Applied Physics B. 2013; 112(4):521-7.

[24]. Upputuri PK, Periyasamy V, Kalva SK, Pramanik M. A High-performance compact photoacoustic tomography system for in vivo small-animal brain imaging. Journal of Visualized Experiments. 2017; (124):e55811.

[25]. Sivasubramanian K, Periyasamy V, Wen KK, Pramanik M. Optimizing light delivery through fiber bundle in photoacoustic imaging with clinical ultrasound system: Monte Carlo simulation and experimental validation. J Biomed Opt. 2017; 22(4):041008.

[26]. Tang J, Coleman JE, Dai X, Jiang H. Wearable 3-D Photoacoustic Tomography for Functional Brain Imaging in Behaving Rats. Sci Rep. 2016; 6:25470.

[27]. Deng Z, Li W, Li C. Slip-ring-based multi-transducer photoacoustic tomography system. Opt Lett. 2016; 41(12):2859-62.

[28]. Wiraja C, Mathiyazhakan M, Movahedi F, Upputuri PK, Cheng Y, Pramanik M, Yang L, David B, Xu C. Near-infrared light-sensitive liposomes for enhanced plasmid DNA transfection. Bioengineering & Translational Medicine. 2016; 1(3):357-64.

[29]. Upputuri PK, Pramanik M. Performance characterization of low-cost, high-speed, portable pulsed laser diode photoacoustic tomography (PLD-PAT) system. Biomed Opt Express. 2015; 6(10):4118-29.

[30]. Xia W, Piras D, Singh MKA, van Hespen JCG, van Leeuwen TG, Steenbergen W, Manohar S. Design and evaluation of a laboratory prototype system for 3D photoacoustic full breast tomography. Biomed Opt Express. 2013; 4(11):2555-69.

[31]. Yang X, Maurudis A, Gamelin J, Aguirre A, Zhu Q, Wang LV. Photoacoustic tomography of small animal brain with a curved array transducer. J Biomed Opt. 2009; 14(5):054007.

[32]. Park B, Lee H, Upputuri PK, Pramanik M, Kim D, Kim C. Super-resolution photoacoustic microscopy using near-field localization by a plasmonic metal nanoaperture: a simulation study. IEEE Journal of Selected Topics in Quantum Electronics. 2019 (In Press).

[33]. Cao R, Li J, Ning B, Sun N, Wang T, Zuo Z, Hu S. Functional and oxygen-metabolic photoacoustic microscopy of the awake mouse brain. Neuroimage. 2017; 150:77-87.

[34]. Park K, Kim JY, Lee C, Jeon S, Lim G, Kim C. Handheld Photoacoustic Microscopy Probe. Sci Rep. 2017; 7(1):13359.

[35]. Qi W, Jin T, Rong J, Jiang H, Xi L. Inverted multiscale optical resolution photoacoustic microscopy. Journal of biophotonics. 2017; 10(12):1580-5.

[36]. Kiri Lee EC, Seungrag Lee, Tae Joong Eom. High-speed dual-layer scanning photoacoustic microscopy using focus tunable lens modulation at resonant frequency. Opt Express. 2017; 25(22):10.

[37]. Hajireza P, Shi W, Bell K, Paproski RJ, Zemp RJ. Non-Interferometric Photoacoustic Remote Sensing Microscopy. Light: Science & Applications. 2017; 6:e16278.

[38]. Moothanchery M, Pramanik M. Performance Characterization of a Switchable Acoustic and Optical Resolution Photoacoustic Microscopy System. Sensors. 2017; 17(2):357.

[39]. Moothanchery M, Seeni RZ, Xu C, Pramanik M. In vivo studies of transdermal nanoparticle delivery with microneedles using photoacoustic microscopy. Biomed Opt Express. 2017; 8(12):5483-92.

[40]. Upputuri PK, Krishnan M, Pramanik M. Microsphere enabled sub-diffraction limited optical-resolution photoacoustic microscopy: a simulation study. J Biomed Opt. 2017; 22(4):045001.

[41]. Murray TW, Haltmeier M, Berer T, Leiss-Holzinger E, Burgholzer P. Super-resolution photoacoustic microscopy using blind structured illumination. Optica. 2017; 4(1):17-22.

[42]. Lee S, Kwon O, Jeon M, Song J, Shin S, Kim H, Jo M, Rim T, Doh J, Kim S, Son J, Kim Y, Kim C. Super-resolution visible photoactivated atomic force microscopy. Light: Science & Applications. 2017; 6(11):e17080.

[43]. Strohm EM, Moore MJ, Kolios MC. Single Cell Photoacoustic Microscopy: A Review. IEEE Journal of Selected Topics in Quantum Electronics. 2016; 22(3):6801215.

[44]. Schwarz M, Buehler A, Aguirre J, Ntziachristos V. Three-dimensional multispectral optoacoustic mesoscopy reveals melanin and blood oxygenation in human skin in vivo. Journal of biophotonics. 2016; 9(1-2):55-60.

[45]. Yang X, Xie H, Alonas E, Liu Y, Chen X, Santangelo PJ, Ren Q, Xi P, Jin D. Mirror-enhanced super-resolution microscopy. Light, science & applications. 2016; 5(6):e16134.

[46]. Kim JY, Lee C, Park K, Han S, Kim C. High-speed and high-SNR photoacoustic microscopy based on a galvanometer mirror in non-conducting liquid. Sci Rep. 2016; 6:34803.

[47]. Yao J, Wang L, Yang JM, Maslov KI, Wong TTW, Li L, Huang CH, Zou J, Wang LV. High-speed label-free functional photoacoustic microscopy of mouse brain in action. Nat Methods. 2015; 12(5):407-10.

[48]. Wang T, Cao R, Ning B, Dixon AJ, Hossack JA, Klibanov AL, Zhou Q, Wang A, Hu S. All-optical photoacoustic microscopy based on plasmonic detection of broadband ultrasound. Appl Phys Lett. 2015; 107(15):153702.

[49]. Wang T, Nandy S, Salehi HS, Kumavor PD, Zhu Q. A low-cost photoacoustic microscopy system with a laser diode excitation. Biomed Opt Express. 2014; 5(9):3053-58.

[50]. Upputuri PK, Wen Z-B, Wu Z, Pramanik M. Super-resolution photoacoustic microscopy using photonic nanojets: a simulation study. J Biomed Opt. 2014; 19(11):116003.

[51]. Cai D, Li G, Xia D, Li Z, Guo Z, Chen S-L. Synthetic aperture focusing technique for photoacoustic endoscopy. Opt Express. 2017; 25(17):20162-71.

[52]. Xiao J, Li Y, Jin W, Peng K, Zhu Z, Wang B. Photoacoustic endoscopy with hollow structured lens-focused polyvinylidine fluoride transducer. Appl Opt. 2016; 55(9):2301-5.

[53]. Yang JM, Li C, Chen R, Rao B, Yao J, Yeh CH, Danielli A, Maslov K, Zhou Q, Shung KK, Wang LH. Optical-resolution photoacoustic endomicroscopy in vivo. Biomed Opt Express. 2015; 6(3):918-32.

[54]. Yang JM, Maslov K, Yang HC, Zhou QF, Shung KK, Wang LV. Photoacoustic endoscopy. Opt Lett. 2009; 34(10):1591-93.

[55]. Jiang Y, Upputuri PK, Xie C, Lyu Y, Zhang L, Xiong Q, Pramanik M, Pu K. Broadband Absorbing Semiconducting Polymer Nanoparticles for Photoacoustic Imaging in Second Near-Infrared Window. Nano Lett. 2017; 17(8):4964-9.

[56]. Zhou Y, Wang D, Zhang Y, Chitgupi U, Geng J, Wang Y, Zhang Y, Cook TR, Xia J, Lovell JF. A Phosphorus Phthalocyanine Formulation with Intense Absorbance at 1000 nm for Deep Optical Imaging. Theranostics. 2016; 6(5):688-97.

[57]. Han S, Lee C, Kim S, Jeon M, Kim J, Kim C. In vivo virtual intraoperative surgical photoacoustic microscopy. Appl Phys Lett. 2013; 103(20):203702.

[58]. Song L, Maslov K, Bitton R, Shung KK, Wang LV. Fast 3-D dark-field reflection-mode photoacoustic microscopy in vivo with a 30-MHz ultrasound linear array. J Biomed Opt. 2008; 13(5):054028.

[59]. Zhang HF, Maslov K, Stoica G, Wang LV. Functional photoacoustic microscopy for high-resolution and noninvasive in vivo imaging. Nat Biotechnol. 2006; 24(7):848-51.

[60]. Maslov K, Stoica G, Wang LV. In vivo dark-field reflection-mode photoacoustic microscopy. Opt Lett. 2005; 30(6):625-7.

[61]. Lin L, Zhang P, Xu S, Shi J, Li L, Yao J, Wang L, Zou J, Wang LV. Handheld optical-resolution photoacoustic microscopy. J Biomed Opt. 2017; 22(4):041002.

[62]. Jin T, Guo H, Jiang H, Ke B, Xi L. Portable optical resolution photoacoustic microscopy (pORPAM) for human oral imaging. Opt Lett. 2017; 42(21):4434-7.

[63]. Yang X, Jiang B, Song X, Wei J, Luo Q. Fast axial-scanning photoacoustic microscopy using tunable acoustic gradient lens. Opt Express. 2017; 25(7):7349-57.

[64]. Park S, Vial J-C, Kyhm K. Optical sectioning in optical resolution photo acoustic microscopy. Opt Express. 2017; 25(16):18917-28.

[65]. Chen S-L, Guo LJ, Wang X. All-optical photoacoustic microscopy. Photoacoustics. 2015; 3(4):143-50.

[66]. Li M-L, Wang P-H, editors. Optical resolution photoacoustic microscopy using a Blu-ray DVD pickup head. Proc Spie; 2014: SPIE; 894315.

[67]. Hu S, Maslov K, Wang LV. Second-generation optical-resolution photoacoustic microscopy with improved sensitivity and speed. Opt Lett. 2011; 36(7):1134-36.

[68]. Ku G, Maslov K, Li L, Wang LV. Photoacoustic microscopy with 2-microm transverse resolution. J Biomed Opt. 2011; 15(2):021302.

[69]. Yao J, Wang LV. Sensitivity of photoacoustic microscopy. Photoacoustics. 2014; 2(2):87-101.

[70]. Yang J-M, Maslov K, Chen R, Yang H-C, Zhou Q, Shung KK, Wang LV, editors. Volumetric photoacoustic endoscopy of internal organs: a phantom and in situ study. Proc Spie; 2010; 75640D.

[71]. Wang X, Ku G, Wegiel MA, Bornhop DJ, Stoica G, Wang LV. Noninvasive photoacoustic angiography of animal brains in vivo with near-infrared light and an optical contrast agent. Opt Lett. 2004; 29(27):730-02.

[72]. Zeng L, Liu G, Yang D, Ji X. 3D-visual laser-diode-based photoacoustic imaging. Opt Express. 2012; 20(2):1237-46.

[73]. Su S-Y, Li P-C. Coded excitation for photoacoustic imaging using a high-speed diode laser. Opt Express. 2011; 19(2):1174-82.

[74]. Allen JS, Beard P. Pulsed near-infrared laser diode excitation system for biomedical photoacoustic imaging. Opt Lett. 2006; 31(23):3462-64.

[75]. Kolkman RGM, Steenbergen W, van Leeuwen TG. In vivo photoacoustic imaging of blood vessels with a pulsed laser diode. Lasers Med Sci. 2006; 21(3):134-9.

[76]. Yao Q, Ding Y, Liu G, Zeng L. Low-cost photoacoustic imaging systems based on laser diode and light-emitting diode excitation. J Innov Opt Heal Sci. 2017; 10(04):1730003.

[77]. Allen JT, Beard CP. High power visible light emitting diodes as pulsed excitation sources for biomedical photoacoustics. Biomed Opt Express. 2016; 7(3):1260-70.

[78]. Skov Hansen R, editor Using high-power light emitting diodes for photoacoustic imaging. Proc Spie; 2011; 79680A.

[79]. Upputuri PK, Pramanik M. Dynamic in vivo imaging of small animal brain using pulsed laser diode-based photoacoustic tomography system. J Biomed Opt. 2017; 22(9):090501.

[80]. Daoudi K, van den Berg PJ, Rabot O, Kohl A, Tisserand S, Brands P, Steenbergen W. Handheld probe integrating laser diode and ultrasound transducer array for ultrasound/photoacoustic dual modality imaging. Opt Express. 2014; 22(21):26365-74.

[81]. Sivasubramanian K, Pramanik M. High frame rate photoacoustic imaging at 7000 frames per second using clinical ultrasound system. Biomed Opt Express. 2016; 7(2):312-23.

[82]. Arabul MU, Heres M, Rutten MC, van Sambeek MR, van de Vosse FN, Lopata RG. Toward the detection of intraplaque hemorrhage in carotid artery lesions using photoacoustic imaging. J Biomed Opt. 2017; 22(4):41010.

[83]. Erfanzadeh M, Kumavor PD, Zhu Q. Laser scanning laser diode photoacoustic microscopy system. Photoacoustics. 2018; 9:1-9.

[84]. Guo H, Song C, Xie H, Xi L. Photoacoustic endomicroscopy based on a MEMS scanning mirror. Opt Lett. 2017; 42(22):4615-8.

[85]. Kim JY, Lee C, Park K, Lim G, Kim C. Fast optical-resolution photoacoustic microscopy using a 2-axis water-proofing MEMS scanner. Sci Rep. 2015; 5:07932.

[86]. Yang H, Xi L, Samuelson S, Xie H, Yang L, Jiang H. Handheld miniature probe integrating diffuse optical tomography with photoacoustic imaging through a MEMS scanning mirror. Biomed Opt Express. 2013; 4(3):427-32.

[87]. Yao J, Huang C-H, Wang L, Yang J-M, Gao L, Maslov KI, Zou J, Wang LV. Wide-field fast-scanning photoacoustic microscopy based on a water-immersible MEMS scanning mirror. J Biomed Opt. 2012; 17(8):0805051.

[88]. Beard P. Biomedical photoacoustic imaging. Interface Focus. 2011; 1(4):602-31.

[89]. Zhang E, Laufer J, Beard P. Backward-mode multiwavelength photoacoustic scanner using a planar Fabry–Perot polymer film ultrasound sensor for high-resolution three-dimensional imaging of biological tissues. Appl Opt. 2008; 47(4):561-77.

[90]. Strohm EM, Berndl ES, Kolios MC. High frequency label-free photoacoustic microscopy of single cells. Photoacoustics. 2013; 1(3-4):49-53.

[91]. Hou Y, Huang SW, Ashkenazi S, Witte R, O'Donnell M. Thin polymer etalon arrays for high-resolution photoacoustic imaging. J Biomed Opt. 2008; 13(6):064033.

[92]. Zhang J, Pun SH, Yu Y, Gao D, Wang J, Mak PU, Lei KF, Cheng C-H, Yuan Z. Development of a multi-band photoacoustic tomography imaging system based on a capacitive micromachined ultrasonic transducer array. Appl Opt. 2017; 56(14):4012-8.

[93]. Warshavski O, Meynier C, Senegond N, Chatain P, Rebling J, Razansky D, Felix N, Nguyen-Dinh A, editors. Experimental evaluation of cMUT and PZT transducers in receive only mode for photoacoustic imaging. Proc Spie; 2016; 970830.

[94]. Kothapalli SR, Ma TJ, Vaithilingam S, Oralkan O, Khuri-Yakub BT, Gambhir SS. Deep Tissue Photoacoustic Imaging Using a Miniaturized 2-D Capacitive Micromachined Ultrasonic Transducer Array. IEEE Trans Biomed Eng. 2012; 59(5):1199-204.

[95]. Awasthi N, Kalva SK, Pramanik M, Yalavarthy PK. Vector extrapolation methods for accelerating iterative reconstruction methods in limited-data photoacoustic tomography. J Biomed Opt. 2018; 23(4):041204.

[96]. Gutta S, Kadimesetty VS, Kalva SK, Pramanik M, Ganapathy S, Yalavarthy PK. Deep neural network-based bandwidth enhancement of photoacoustic data. J Biomed Opt. 2017; 22(11):116001.

[97]. Prakash J, Raju AS, Shaw CB, Pramanik M, Yalavarthy PK. Basis pursuit deconvolution for improving model-based reconstructed images in photoacoustic tomography. Biomed Opt Express. 2014; 5(5):1363-77.

[98]. Shaw CB, Prakash J, Pramanik M, Yalavarthy PK. Least squares QR-based decomposition provides an efficient way of computing optimal regularization parameter in photoacoustic tomography. J Biomed Opt. 2013; 18(8):080501.

[99]. Huang H, Bustamante G, Peterson R, Ye JY. An adaptive filtered back-projection for photoacoustic image reconstruction. Med Phys. 2015; 42(5):2169-78.

[100]. Haltmeier M, Neumann L, Rabanser S. Single-stage reconstruction algorithm for quantitative photoacoustic tomography. Inverse Problems. 2015; 31(6):065005.

[101]. Liu L, Tao C, Liu X, Deng M, Wang S, Liu J. Photoacoustic tomography from weak and noisy signals by using a pulse decomposition algorithm in the time-domain. Opt Express. 2015; 23(21):26969-77.

[102]. Wang D, Wang Y, Zhou Y, Lovell JF, Xia J. Coherent-weighted three-dimensional image reconstruction in linear-array-based photoacoustic tomography. Biomed Opt Express. 2016; 7(5):1957-65.

[103]. Li G, Li L, Zhu L, Xia J, Wang LV. Multiview Hilbert transformation for full-view photoacoustic computed tomography using a linear array. J Biomed Opt. 2015; 20(6):066010.

[104]. Cao M, Yuan J, Du S, Xu G, Wang X, Carson PL, Liu X. Full-view photoacoustic tomography using asymmetric distributed sensors optimized with compressed sensing method. Biomedical Signal Processing and Control. 2015; 21:19-25.

[105]. Kalva SK, Pramanik M. Experimental validation of tangential resolution improvement in photoacoustic tomography using a modified delay-and-sum reconstruction algorithm. J Biomed Opt. 2016; 21(8):086011.

[106]. Pramanik M. Improving tangential resolution with a modified delay-and-sum reconstruction algorithm in photoacoustic and thermoacoustic tomography. J Opt Soc Am A. 2014; 31(3):621-7.

[107]. American National Standard for Safe Use of Lasers ANSI Z136.1-2007 (American National Standards Institute, Inc., New York, NY, 2007).

[108]. Ku G, Wang X, Stoica G, Wang LV. Multiple-bandwidth photoacoustic tomography. Phys Med Biol. 2004; 49(7):1329-38.

[109]. Ma R, Taruttis A, Ntziachristos V, Razansky D. Multispectral optoacoustic tomography (MSOT) scanner for whole-body small animal imaging. Opt Express. 2009; 17(24):21414-26.

[110]. Oraevsky AA, Wang LV, Klosner M, Chan G, Wu C, Heller DF, Su R, Ermilov S, Brecht HP, Ivanov V, Talole P, Lou Y, Anastasio M, Oraevsky A, editors. Advanced laser system for 3D optoacoustic tomography of the breast. Proc Spie; 2016; 97085B.

[111]. Oraevsky AA, Wang LV, Vogt WC, Jia C, Wear KA, Garra BS, Pfefer J, editors. Quantitative assessment of photoacoustic tomography systems integrating clinical ultrasound transducers using novel tissue-simulating phantoms. Proc Spie; 2015; 932333.

[112]. Upputuri PK, Pramanik M. Pulsed laser diode based optoacoustic imaging of biological tissues. Biomedical Physics & Engineering Express. 2015; 1(4):045010-7.

[113]. Zhang J, Zhen X, Upputuri PK, Pramanik M, Chen P, Pu K. Activatable photoacoustic nanoprobes for in vivo ratiometric imaging of peroxynitrite. Adv Mater. 2017; 29(6):1604764.

[114]. Xie C, Upputuri PK, Zhen X, Pramanik M, Pu K. Self-Quenched semiconducting polymer nanoparticles for amplified in vivo photoacoustic imaging. Biomaterials. 2017; 119:1-8.

[115]. Jiang Y, Cui D, Fang Y, Upputuri PK, Pramanik M, Ding D, Pu K. Amphiphilic semiconducting polymer as multifunctional nanocarrier for fluorescence/photoacoustic imaging guided chemo-photothermal therapy. Biomaterials. 2017; 145:168-77.

[116]. Huang S, Upputuri PK, Liu H, Pramanik M, Wang M. A dual-functional benzobisthiadiazole derivative as an effective theranostic agent for near-infrared photoacoustic imaging and photothermal therapy. Journal of Materials Chemistry B. 2016; 4(9):1696-703.

[117]. Upputuri PK, Huang S, Wang M, Pramanik M, editors. A dual function theranostic agent for near-infrared photoacoustic imaging and photothermal therapy. Proc Spie; 2016; 97230Y.

[118]. Burton NC, Patel M, Morscher S, Driessen WH, Claussen J, Beziere N, Jetzfellner T, Taruttis A, Razansky D, Bednar B, Ntziachristos V. Multispectral opto-acoustic tomography (MSOT) of the brain and glioblastoma characterization. Neuroimage. 2013; 65(2):522-8.

[119]. Lvming Zeng, Guodong Liu, Diwu Yang, Ji X. Cost-efficient laser-diode-induced optical-resolution photoacoustic microscopy for two-dimensional/three-dimensional biomedical imaging. J Biomed Opt. 2014; 19(7):076017.

[120]. Zeng L, Piao Z, Huang S, Jia W, Chen Z. Label-free optical-resolution photoacoustic microscopy of superficial microvasculature using a compact visible laser diode excitation. Opt Express. 2015; 23(24):31026-33.

[121]. Hariri A, Fatima A, Mohammadian N, Mahmoodkalayeh S, Ansari MA, Bely N, Avanaki MR. Development of low-cost photoacoustic imaging systems using very low-energy pulsed laser diodes. J Biomed Opt. 2017; 22(7):075001.

[122]. Daoudi K, Van den Berg PJ, Rabot O, Kohl A, Tisserand S, Brands P, Steenbergen W, editors. Handheld probe for portable high frame photoacoustic/ultrasound imaging system. Proc Spie; 2013; 85212l.

[123]. Dai X, Yang H, Jiang H. In vivo photoacoustic imaging of vasculature with a low-cost miniature light emitting diode excitation. Opt Lett. 2017; 42(7):1456-9.

[124]. Allen TJ, Beard PC, editors. Light emitting diodes as an excitation source for biomedical photoacoustics. Proc Spie; 2013; 85811F.

[125]. Adachi Y, Hoshimiya T. Photoacoustic Imaging with Multiple-Wavelength Light-Emitting Diodes. Jpn J Appl Phys. 2013; 52(7S):07HB6.

Table-1: Performance comparison between pulsed laser diode based PAT system and conventional PAT system. Reprinted from Ref. [29].

S.No.	Imaging and laser parameter		OPO - PAT system parameters	PLD - PAT system parameters
1	Spatial resolution	2.25 MHz	381 μm	384 μm
2	Imaging speed		30 sec per image	3 sec per image
3	SNR	2.25 MHz	28 (30 sec)	29 (3 sec) & 84 (30 sec)
4	Imaging depth		~4 cm (120 sec scan time)	~2 cm (SNR 10 at 30 sec)
5	Image quality	3 sec	Not Acceptable	Acceptable
		30 sec	Good	Good
6	Laser dimensions		775 x 178 x 190 mm	110 X 60 X 36 mm
7	Pulse width		5 ns	136 ns
8	Portability		Active optical table needed	Yes
9	Pulse repetition-rate		10 Hz	7000 Hz
10	Energy per pulse at laser window		~100 mJ	~1.45 mJ
11	Laser weight		~100 Kg	~150 gm
12	Price		~90-140k USD	~15-25k USD

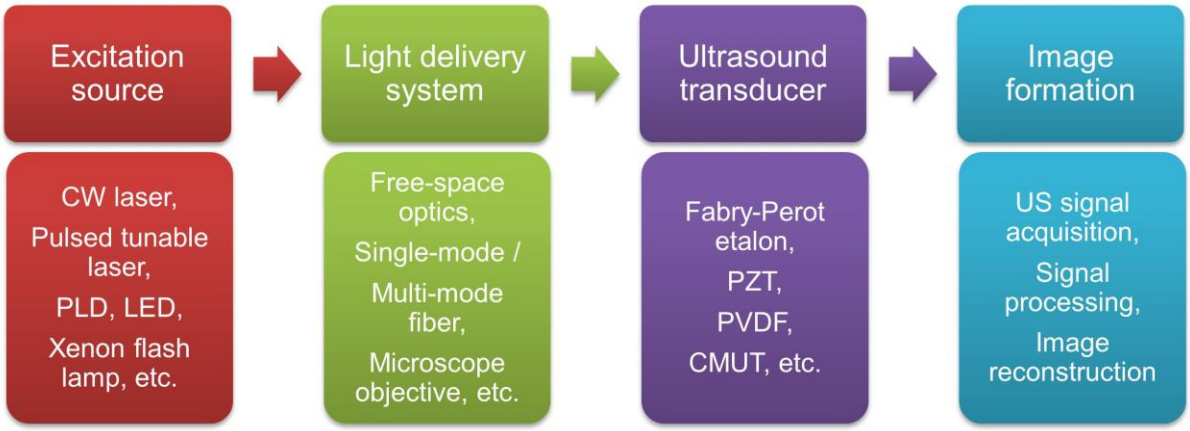

Fig. 1 The main components of photoacoustic imaging (PAI) systems.

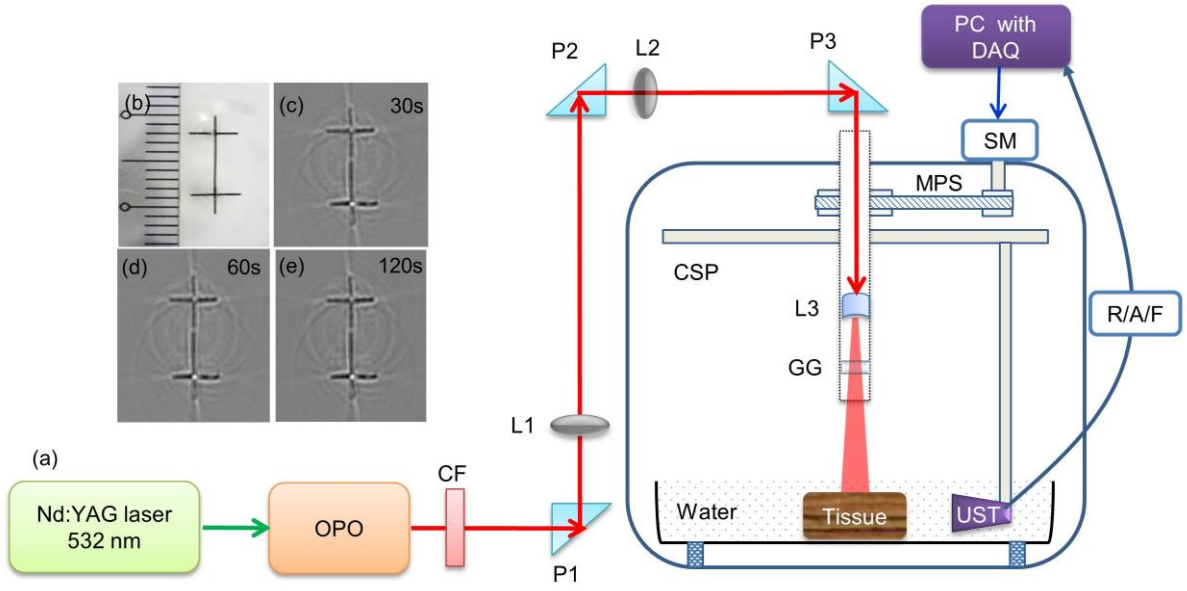

Fig. 2 (a) Diagram of the conventional PAT system. Excitation source is OPO pumped by 532 nm Nd:YAG laser. Where OPO - optical parametric oscillator, CSP - circular scanner, MPS – stepper motor pulley system, DAQ - data acquisition card, SM - stepper motor, R/A/F – photoacoustic signal amplifier unit, UST - US detector or transducer, CF – 532 nm colour filter, GG – ground glass or optical diffuser, P - right angle prism with anti-reflection coating, L1 & L2 - focusing lenses, L3 - diverging lens. Photoacoustic tomography of the phantom (b) prepared using horse hair : Images acquired using 2.25 MHz transducer at (c) 30 sec, (d) 60 sec, (e) 120 sec. Reprinted from Ref [29].

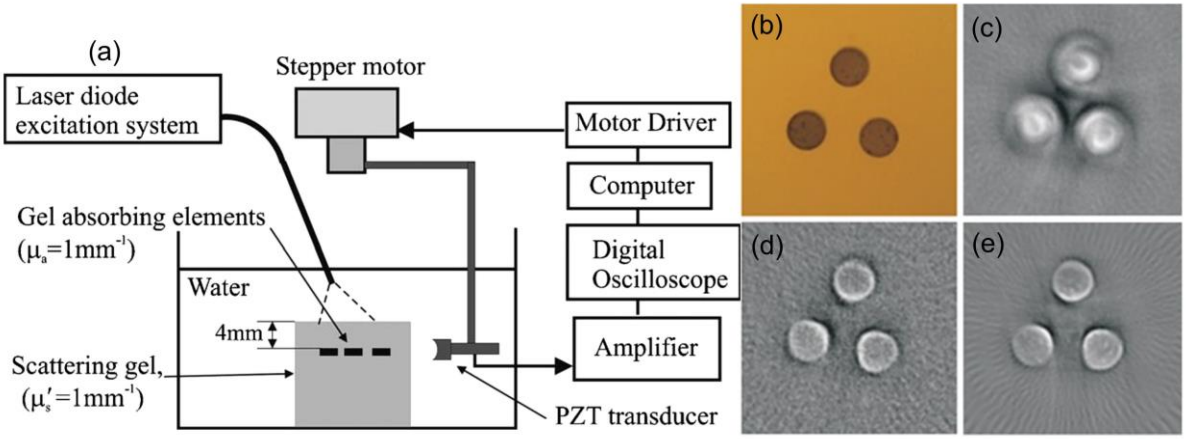

Fig. 3 (a) Cylindrical scanning PLD-PAT system, (b) Photograph of the phantom, (c) and (d) PA images obtained using (c) 500 ns PLD, (d) 65 ns PLD, and (e) 7 ns Nd:YAG laser. Reprinted from Ref [74].

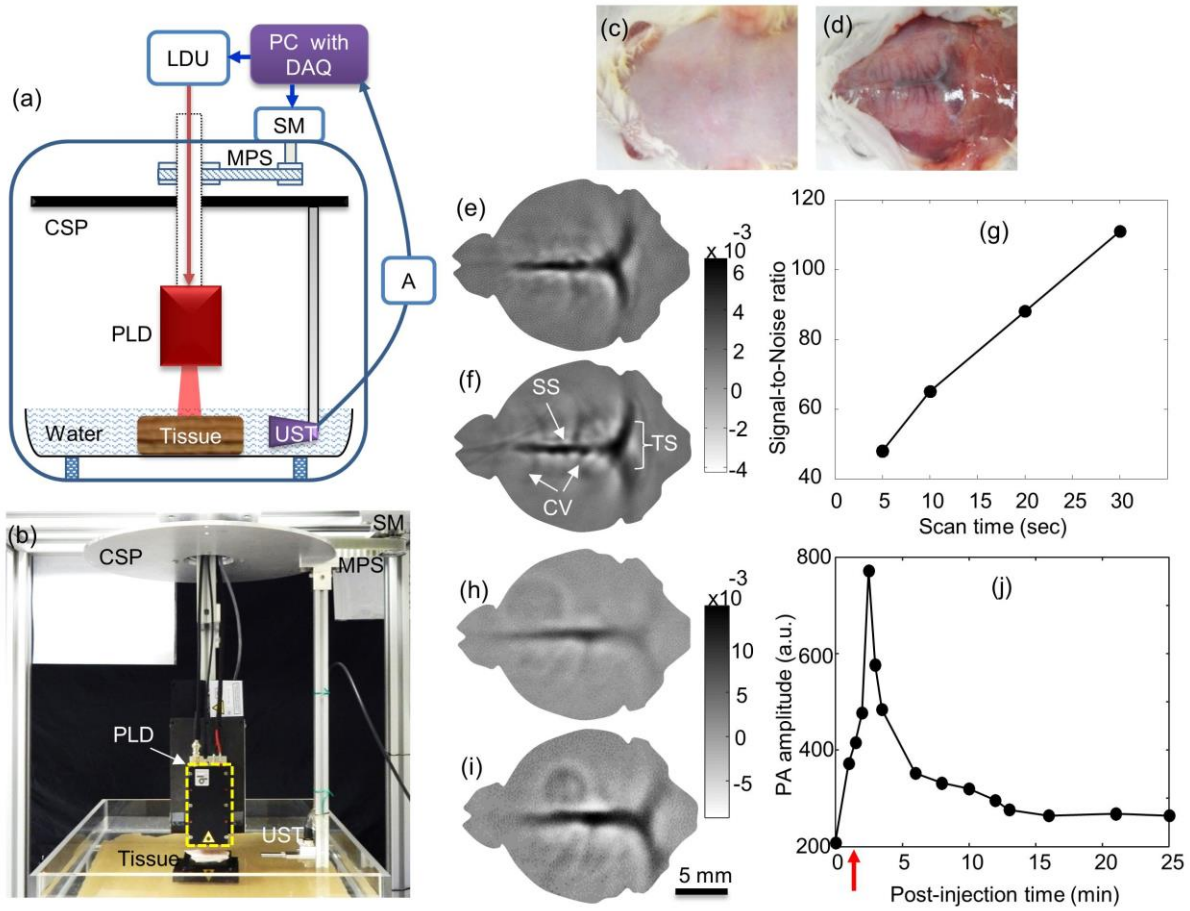

Fig. 4 (a) Diagram, and (b) picture of the PLD based PAT system. Where PLD - Pulsed laser diode, LDU - Laser driver unit, A - PA signal amplifier, CSP - Circular scanning plate, MPS - Motor pulley system, SM - Stepper motor, DAQ - Data acquisition card, UST - Ultrasound detector or transducer. Reprinted from Ref [29]. Noninvasive PLD-PAT images of rat brain vasculature: picture of the brain cortex (c) before and (d) after removing the scalp. Brain vasculature images obtained by reconstructing the A-line data acquired in (e) 5 sec, and (f) 30 sec scan time. Where SS is the sagittal sinus, TS is the transverse sinus, CV is the cerebral veins. (g) signal-to-noise ratio of *in vivo* brain images at different scan times. *In vivo* PLD-PAT brain imaging with ICG intravenously injected in to rat brain: (h) image before injecting ICG, (i) Image 2 min after injecting ICG. (j) Graph shows the quantification of ICG signal

during 25 min after injection. The arrow indicates the time at which ICG was injected in the tail vein. Reprinted from Ref [79].

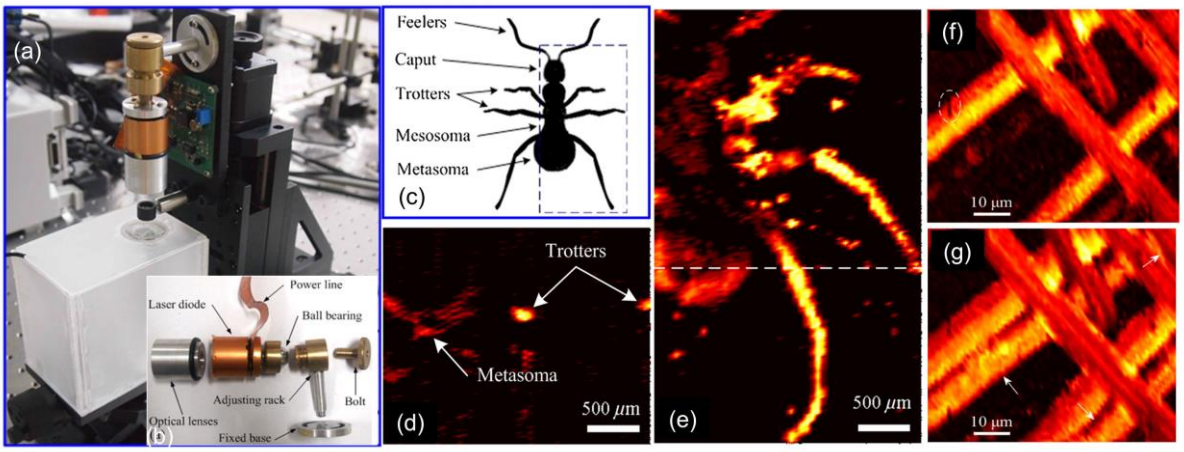

Fig. 5 (a) Picture of the near-infrared (NIR) pulsed laser diode based PAM system, (b) Picture of the individual components of the system, (c) Anatomic schematic of an ant, (d) Two-dimensional PA B-scan image along the dashed line in (c), (e) 2-D photoacoustic MAP image of the ant. Reprinted from Ref [119]. Visible (VIS) PLD based PAM imaging : (f) microscopic image of the carbon fiber network, (g) MAP image by depth-scanning. Here carbon fibers and surface flaws are indicated by arrows and ellipses, respectively. Reprinted from Ref [120].

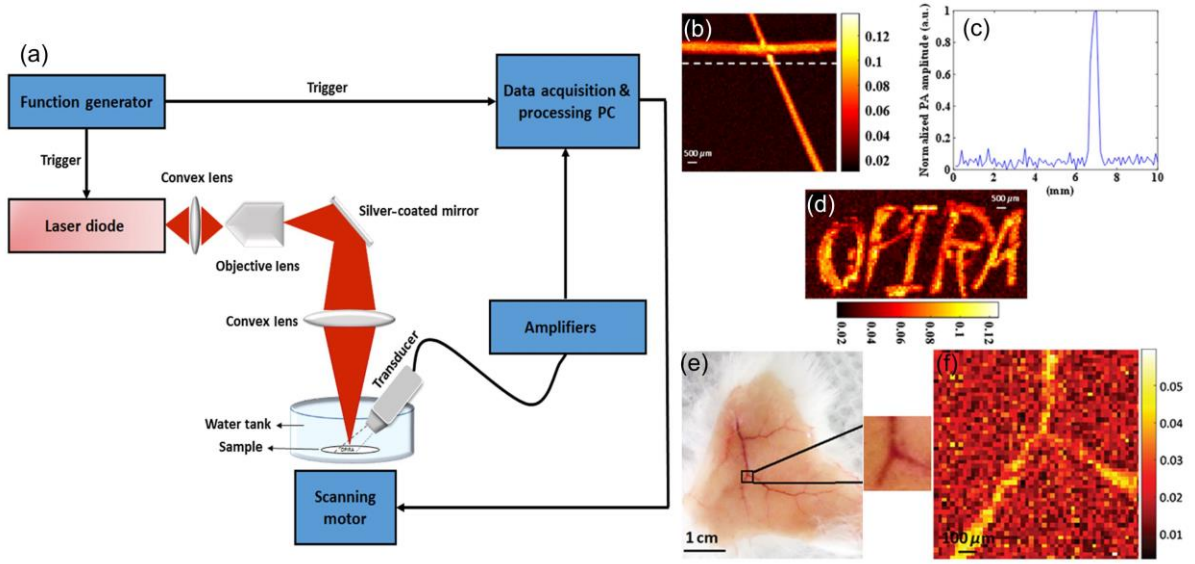

Fig. 6 (a) Diagram of the reflection mode PLD-PAM system, (b) PAM image of a phantom made with black tape, (c) intensity profile along the dotted line across the PA image in (b), and (d) PAM image of the word “OPIRA” made of black tape, *Ex vivo* results on mouse: (e) photograph of a mouse skin on which the ROI is specified, and (f) corresponding PAM image. Reprinted from Ref [121].

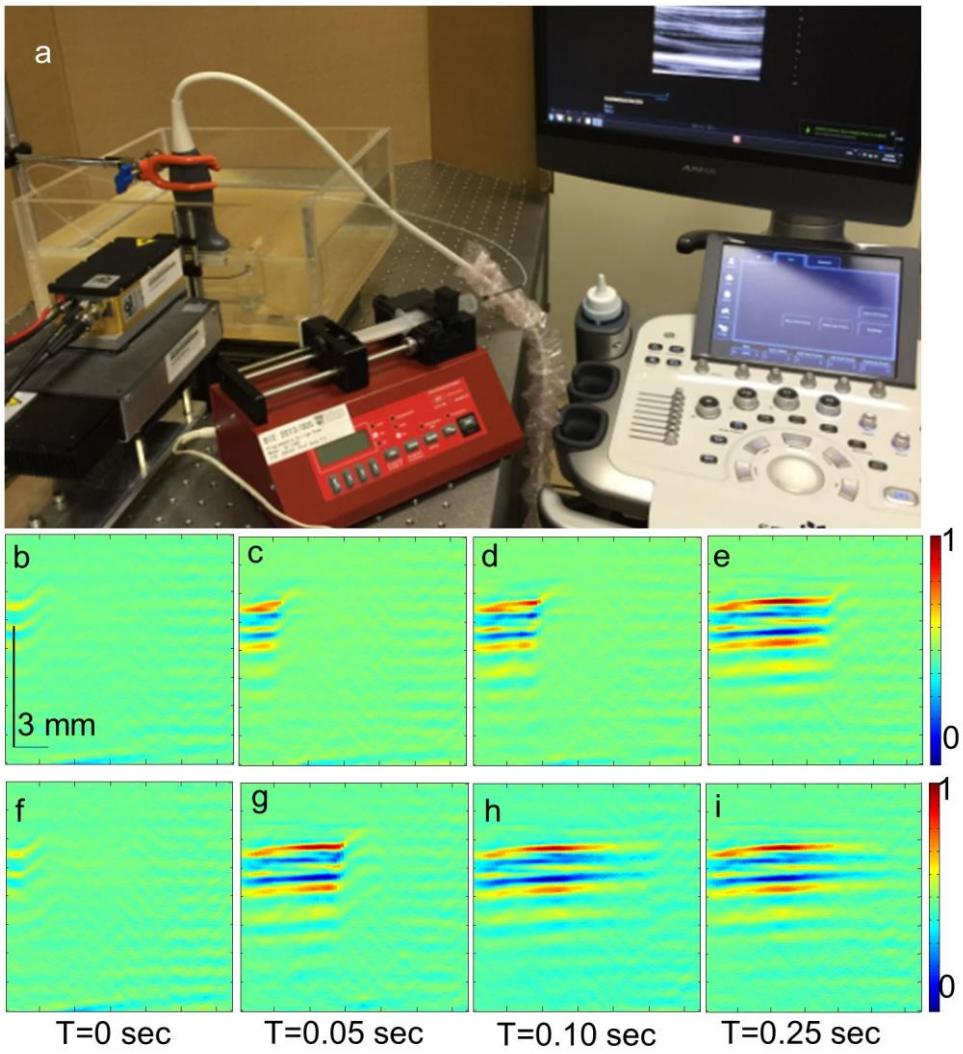

Fig. 7 (a) Picture of the high frame rate PA/US clinical system based on pulsed laser diode. Multiple PA images display the flow of black ink at different times. PA images were acquired at a frame rate of 7k fps. Flow rate was 3 cm/sec (b-e) and 14 cm/sec (f-i). Reprinted from Ref [81].

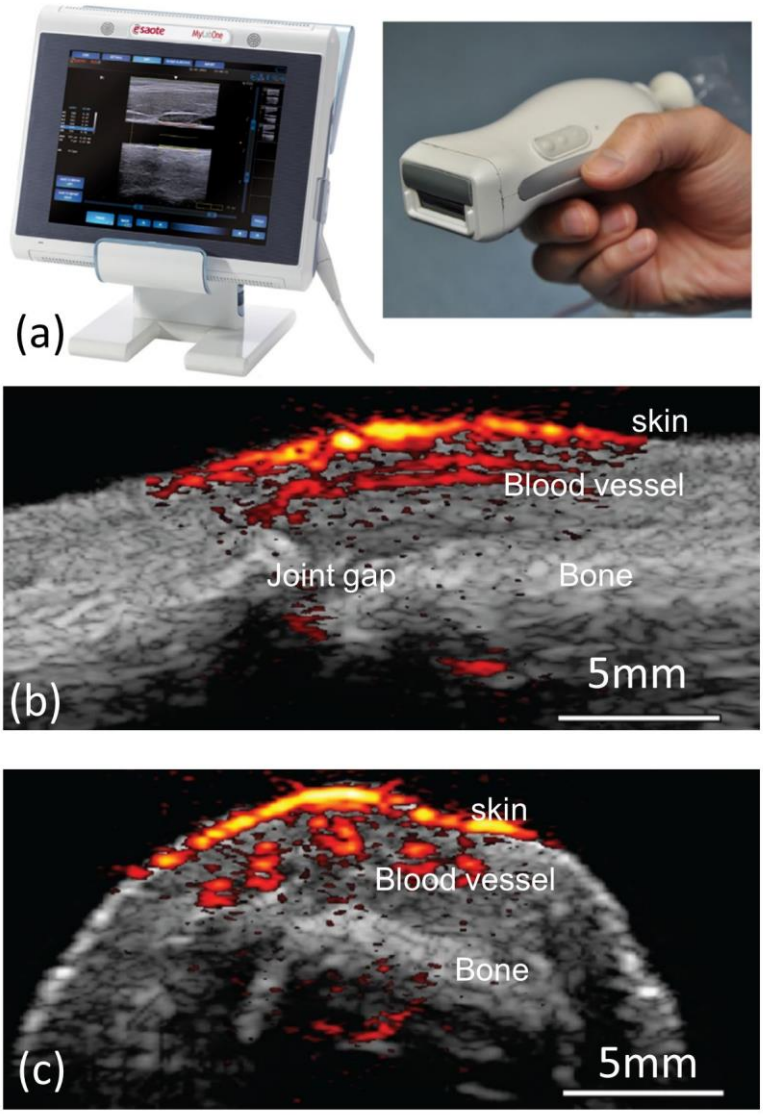

Fig. 8(a) Picture of the portable photoacoustic / ultrasound scanner. Pulsed laser diode (PLD) excitation source is smartly incorporated inside the US probe. Overlaid images of a human finger joint in sagittal (b) and transverse (c) planes. Reprinted from Ref [80].

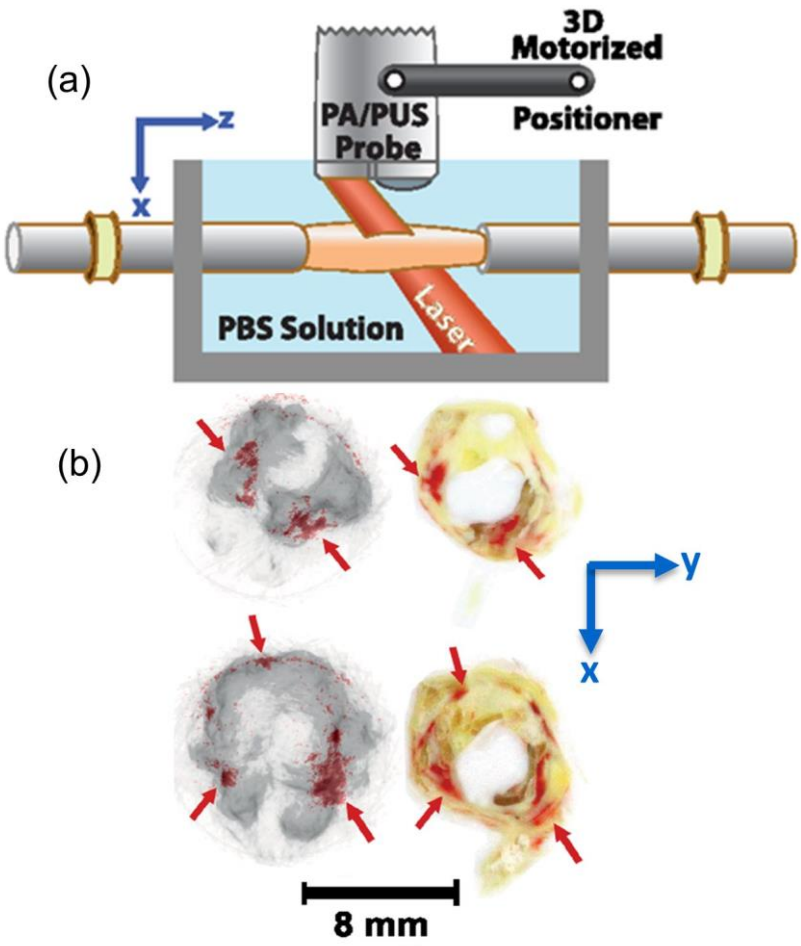

Fig. 9 Illustration of the PLD based PA/US dual-modality system. The sample was immersed into phosphate-buffered-saline (PBS) solution. The imaging probe was positioned in the cross-section of the sample for PA imaging. (b) Pictures of histology sections and the corresponding cross-sections in overlaid PA-PUS images of plaques. Gray colour represents the ultrasound signals and overlaid red colour represent the PA signals. The red arrows indicate the blood content inside the plaques in the histology pictures and the corresponding PA signals in overlaid PA/PUS images. Reprinted from Ref [82].